



A novel infrared imager for studies of hydroxyl and oxygen nightglow emissions in the mesopause above northern Scandinavia

Peter Dalin¹, Urban Brändström¹, Johan Kero¹, Peter Voelger¹, Takanori Nishiyama², Trond Trondsen³, Devin Wyatt³, Craig Unick³, Vladimir Perminov⁴, Nikolay Pertsev⁴, and Jonas Hedin⁵

¹Swedish Institute of Space Physics (IRF), Kiruna, Sweden

²National Institute of Polar Research, Tokyo, Japan

³Keo Scientific Ltd., Calgary, Canada

⁴A.M. Obukhov Institute of Atmospheric Physics, Moscow, Russia

⁵Department of Meteorology, Stockholm University, Stockholm, Sweden

Correspondence: Peter Dalin (pdalin@irf.se)

Received: 2 October 2023 – Discussion started: 15 November 2023

Revised: 26 January 2024 – Accepted: 7 February 2024 – Published: 15 March 2024

Abstract. The paper describes technical characteristics and presents the first scientific results of a novel infrared imaging system (imager) for studies of nightglow emissions coming from the hydroxyl (OH) and molecular oxygen (O₂) layers in the mesopause region (80–100 km) above northern Scandinavia. The OH imager was put into operation in November 2022 at the Swedish Institute of Space Physics in Kiruna (67.86° N, 20.42° E; 400 m altitude). The OH imager records selected emission lines in the OH(3–1) band near 1500 nm to obtain intensity and temperature maps at around 87 km altitude. In addition, the OH imager registers infrared emissions coming from the O₂ IR A-band airglow at 1268.7 nm in order to obtain O₂ intensity maps at a slightly higher altitude, around 94 km. This technique allows the tracing of wave disturbances in both horizontal and vertical domains in the mesopause region. Validation and comparison of the OH(3–1) rotational temperature with collocated lidar and Aura Microwave Limb Sounder (MLS) satellite temperatures are performed. The first scientific results obtained from the OH imager for the first winter season (2022–2023) are discussed.

1 Introduction

Aside from a well-known scattering of sunlight on air molecules (Rayleigh scattering) and particle scattering, the

Earth's atmosphere emits its own radiation 24 h d^{−1}, year-round and on global scales. So-called airglow emissions occur in the mesosphere (50–90 km) and thermosphere (above 90 km). The most prominent airglow emissions are red and green lines of atomic oxygen, ultraviolet and infrared bands of molecular oxygen, hydroxyl (OH) emissions in the infrared part of the spectrum, the yellow emission line of sodium (Na), and ultraviolet and infrared bands of nitric oxide (NO) (e.g., Chamberlain, 1961; Khomich et al., 2008; Savigny, 2017).

Studies of airglow emissions provide important sources of information on the physical and chemical states of the middle and upper atmosphere. In particular, the temperature of emission layers in the middle and upper atmosphere can be determined by analyzing spectral bands and lines of airglow emissions. By analyzing spatial–temporal variations in the emission intensities and/or temperature, one can investigate the short- and long-term dynamical state of the middle and upper atmosphere, which in turn is a hot topic of current atmospheric research (e.g., Fritts and Alexander, 2003; Plougonven and Zhang, 2014; Reid et al., 2014; Wüst et al., 2023; Gavrilov et al., 2024). The key role in the atmospheric dynamical state belongs to waves, a fundamental property of the atmosphere as they transport energy and momentum across great distances (Gossard and Hook, 1975).

Observations of airglow emissions are used to infer parameters of atmospheric waves since temperature and emis-

sion intensity fields in the mesosphere and thermosphere are directly modulated by gravity and planetary waves, solar thermal tides and lunar gravitational tides (e.g., Garcia et al., 1997; Taylor et al., 1997; Pautet et al., 2005; Suzuki et al., 2008; Offermann et al., 2009; Gao et al., 2011; Perminov et al., 2018; Pertsev et al., 2021).

Another very important aspect of atmospheric physics is the long-term monitoring of atmospheric parameters. The scientific community is debating to what extent long-term changes in H₂O, CO₂, N₂O, CH₄ and O₃ (greenhouse gases of anthropogenic and natural origin) contribute to long-term variability in atmospheric temperature. While CO₂ is thought to add to global warming on Earth, it also cools the middle atmosphere (Roble and Dickinson, 1989; Mlynczak et al., 2022). The increased H₂O concentration leads to warmer temperatures due to strong positive water vapor feedback (Dessler et al., 2008). Methane oxidizes in the stratosphere and mesosphere, producing an additional amount of water vapor in the middle atmosphere (Thomas and Olivero, 2001). The global monthly mean atmospheric-methane abundance demonstrates a constant increase since 1987 (https://gml.noaa.gov/ccgg/trends_ch4/, last access: 27 February 2024), which may have caused the observed long-term trend in water vapor in the mesopause. Lübken et al. (2018) have obtained a summer mesopause cooling of ~ 1.2 K per decade for the period of 1960–2008 based on Leibniz Institute Middle Atmosphere (LIMA) and Mesospheric Ice Microphysics And tranSPort (MIMAS) model simulations which included long-term evolutions of the minor atmospheric species CO₂, CH₄, H₂O and O₃. Thus, the long-term temperature trend in the middle atmosphere is a complex function of several atmospheric components. Estimates of temperatures of the middle atmosphere are only possible with the help of remote-sensing instruments. That is why observations of airglow emissions are used for long-term monitoring of the temperature in the mesopause region (Semenov and Shefov, 1999; Espy and Stegman, 2002; Offermann et al., 2010; Ammosov et al., 2014; Kalicinsky et al., 2016; Perminov et al., 2018; Dalin et al., 2020; French et al., 2020).

More than 50 sites conducting spectroscopic and imaging airglow observations are presented at the Network for the Detection of Mesospheric Change (NDMC), which is a global program investigating climate change signals in the mesopause region (<https://ndmc.dlr.de/>, last access: 27 February 2024). Li et al. (2018) have summarized a global distribution of all-sky airglow imager sites (see Table 1 in their paper and references therein). Some of the OH spectrographs and imaging instruments have a narrow field of view of 30° or less, such as the Ground-based Infrared P-branch Spectrometer instrument (GRIPS 6) in Oberpfaffenhofen, Germany (Schmidt et al., 2013); the Aerospace Nightglow Imager 2 (ANI2) in the Andes, Chile (Hecht et al., 2023); and the spectral airglow temperature imager (SATI) in Resolute Bay, Canada (Wiens et al., 1997). A number of OH imaging instruments measure OH emissions in relative units without

mesopause temperature derivations, such as the ANI2; the OH all-sky airglow imager in Kazan, Russia (Li et al., 2018); and the Fast Airglow IMager (FAIM) in Oberpfaffenhofen, Germany (Hannawald et al., 2016). Some of the OH imagers register OH emissions (including temperature derivations) without capturing infrared emissions coming from the O₂ layer, such as the Advanced Mesospheric Temperature Mapper (AMTM) at the South Pole (Pautet et al., 2014) and the Near InfraRed Aurora Camera (NIRAC) in Svalbard, Norway (Nishiyama et al., 2024).

In the present paper, we describe a novel wide-angle infrared imaging instrument (referred to hereafter as the OH imager) capable of registering emissions coming from two emitted layers (OH and O₂) and of deriving the mesopause temperature. The OH imager is the first of its kind installed in northern Scandinavia. The instrument measures infrared emissions of selected lines in the OH(3-1) band at wavelengths near 1.5 μ m to produce intensity and temperature maps in the mesopause region at around 87 km altitude. Additionally, the OH imager records nightglow emissions from the O₂ IR A-band at 1268.7 nm to obtain O₂ emission intensity maps at a slightly higher altitude of about 94 km. Combining data from both layers allows the tracing of wave disturbances in 3-D space, i.e., horizontally and vertically in the mesopause region. The OH imager was installed in November 2022 at the Swedish Institute of Space Physics (IRF) in Kiruna (67.86° N, 20.42° E; 400 m altitude) on the eastern side of the Scandinavian Mountains. Mountain gravity waves occur frequently at the location; thus the OH imager can be utilized to study the influence of such waves on the thermal and dynamical regime of the mesopause region over Kiruna. The OH registrations are part of the long-term research infrastructure commitment of the Kiruna Atmospheric and Geophysical Observatory (KAGO), part of the IRF, whose objective is to provide present and future scientists with long, continuously archived time series of data of the highest possible scientific quality from its set of instruments.

In Sect. 2, we describe the technical characteristics of the OH imager as well as the principle of OH(3-1) rotational temperature measurements. In Sect. 3, the temperature estimation and its uncertainty, calibration, and validation techniques are presented. Validation of OH(3-1) temperatures with the collocated Esrange lidar temperature measurements and a comparison of OH temperatures with simultaneous Aura Microwave Limb Sounder (MLS) satellite temperatures are shown in Sect. 4. In Sect. 5, the first scientific results obtained with the OH imager are discussed. Finally, conclusions are given in Sect. 6.

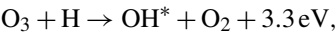
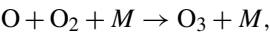
Table 1. The main characteristics of the OH imager in Kiruna.

Parameter	Value
Charge-coupled device (CCD) image sensor	Indium gallium arsenide (InGaAs) focal plane array
CCD format; used for image processing	640 × 512 ; 512 × 512 px
CCD image area	12.80 × 10.24 mm
Pixel size	20 × 20 μm
High full-well pixel capacity at 2 MHz	677, 800 electrons
Quantum efficiency	~ 85 %
Dark current at 2 MHz at −80 °C	21.1 electron px ^{−1} s ^{−1}
Temperature of detector using a Peltier cooler	−80 °C at ambient temperature 21 °C
Digitization	16 bit
Field of view	120°
Filter diameter	76.2 mm
Narrow-band three-cavity filters centered at	
OH(3-1) background (Δλ FWHM)	1521.0 nm (Δλ = 2.2 nm)
OH(3-1) P1(2) line (Δλ FWHM)	1523.7 nm (Δλ = 2.2 nm)
OH(3-1) P1(4) line (Δλ FWHM)	1542.8 nm (Δλ = 2.1 nm)
O2 IR A-band line	1268.7 nm (Δλ = 2.9 nm)
Exposure times for OH and O2 filters	30 and 40 s
Time resolution of the whole cycle	165 s
Spatial resolution of OH measurements at 87 km	0.3 km in the image center
Horizontal coverage at 87 km	300 × 300 km

2 Instrument description

2.1 Theory and basic knowledge

The hydroxyl (OH) airglow emission layer exists in the Earth’s atmosphere between 75 and 100 km, with the highest concentration at about 87 km and the full width at half maximum of about 8–10 km (Baker and Stair, 1988; Savigny, 2017), although both of these parameters of the OH-layer change depending on geolocation and season (Perminov et al., 1999, 2018; Melo et al., 2000; Grygalashvyly et al., 2014). Its rotational–vibrational bands, covering the spectral region from 0.5 to 4.5 μm, result mainly from the chemiluminescent processes (Bates and Nicolet, 1950):



where *M* is a molecule of nitrogen or oxygen and OH* is the OH vibrationally excited molecule. Returning to their ground state, the OH* molecules emit visible and infrared radiation in the spectral range between 500 and 4500 nm.

The OH(8-3) band at 732–742 nm and the OH(6-2) band at 830–845 nm, which are detectable by commercial CCD

cameras, are commonly used in OH airglow observations. However, at high latitudes, auroral emissions (molecular and atomic oxygen lines between 730 and 845 nm) have stronger intensities than those of the OH airglow bands (Christensen et al., 1978; Sivjee et al., 1979). Therefore, measurements of OH nightglow emissions in the short-wave infrared range (SWIR) of the spectrum (900–1700 nm) are preferable in order to minimize auroral contamination at high latitudes (Pautet et al., 2014; Nishiyama et al., 2021). For this purpose, the OH(3-1) band (1470–1550 nm) is used by the OH imager to measure nightglow emissions at high latitudes. It is important to note that the OH(3-1) intensity is 2 orders of magnitude greater than the intensities of the OH(8-3) and OH(6-2) bands. Also, the OH(3-1) emission is less affected by water vapor absorption. All these factors make for a strong preference in choosing the OH(3-1) nightglow observation in Kiruna, as it is located underneath the auroral oval where auroral emissions occur frequently.

2.2 Instrument description

The main component of the OH imager is an infrared camera (Teledyne Princeton Instruments NIRvana 640) equipped

with an indium gallium arsenide (InGaAs) sensor for low-light scientific SWIR imaging applications. The NIRvana 640 camera employs a 640×512 InGaAs array charge-coupled device (CCD), with a spectral response from 900 to 1700 nm. Each pixel has a size of $20 \times 20 \mu\text{m}$. The detector is Peltier-cooled to -80°C to minimize thermally generated noise and thus improve the signal-to-noise ratio. The NIRvana 640 camera has 16-bit digitization, with low readout noise. Other components of the instrument are a SWIR wide-angle primary lens ($\sim 120^\circ$ field of view), an f/1.0 SWIR-optimized telecentric optical system, a thermally stabilized eight-position filter wheel with four narrow-band (three-cavity) interference filters, a brushless DC servo motor drive for the filter wheel, a filter wheel control unit, a power supply, and an instrument control and data acquisition computer. As the center wavelengths of the interference filters are temperature dependent, the filter wheel's closed-loop temperature controller heats the filter wheel cavity to $+23 \pm 0.1^\circ\text{C}$. Along with four narrow-band interference filters, a dark-blocking filter is used to collect data for subtraction of dark-current noise from nighttime measurements. The dark-blocking filter's emissivity is matched to that of the narrow-band interference filters, thus ensuring the dark-current noise collected with it is representative of the dark-current noise present in nighttime measurements. The primary wide-angle lens, telecentric optics and reimaging lens were custom designed and produced for measurements in the SWIR. The reimaging optics consist of a doublet field lens and a combination of a second doublet and an f/1 compound lens in front of the sensor. The optical design of the OH imager inscribes a 120° field-of-view image circle within the short (vertical) dimension of the 640×512 px sensor, resulting in an image circle with a 512 px diameter. The image is therefore cropped to 512×512 px for image-processing purposes. The OH imager was designed and built by Keo Scientific Ltd (<http://keoscientific.com>, last access: 27 February 2024). The main instrument characteristics are summarized in Table 1.

Nightglow observations are restricted to nighttime and twilight (solar elevation angle less than -6.5°) for optimum signal quality. At the arctic location of Kiruna, we are thus able to conduct nightglow measurements from September until the middle of April. The exposure times for the OH, background and dark filters are set to 30 s, whereas the exposure time for the O_2 IR A-band filter is set to 40 s, yielding a complete filter cycle in 2.75 min. This yields the Nyquist frequency of the instrument equal to 0.019 s^{-1} (5.5 min). To avoid aliasing with the Brunt–Väisälä frequency in the mesopause, which is varied around 0.021 s^{-1} (5 min), the instrument is used to resolve the high-frequency range in the gravity-wave spectrum, corresponding to observed wave periods of about 10 min or more. Figure 1 shows the OH imager installed at the Knutstorp observatory (67.86°N , 20.42°E), 2 km north of IRF, on 29 November 2022.

3 Temperature estimation and its uncertainty, error analysis, and calibration technique

3.1 Temperature estimation

The temperature of the air in the mesopause region is determined using the brightness ratio of the two vibrational-rotational lines $\text{P}_1(2)$ and $\text{P}_1(4)$ in the OH(3-1) band. This method is based on the assumption that the rotational level populations are in local thermodynamic equilibrium (LTE). Although the OH vibrational states are excited due to non-thermal processes, the rotational level population is still in LTE due to the long radiative lifetimes of vibrational states (e.g., Savigny, 2017). This method has been proved to be valid and has been applied for several decades in temperature measurements of the mesopause region (Sivjee and Hamwey, 1987; Makhoul et al., 1995; Espy and Stegman, 2002; Pertsev and Perminov, 2008; Suzuki et al., 2008; Offermann et al., 2010; Grygalashvyly et al., 2014; Pautet et al., 2014; Kalicinsky et al., 2016; Perminov et al., 2018).

For the OH rotational temperature estimation, we use Eq. (4) from Pautet et al. (2014). At the same time, we have corrected this equation for the newly estimated Einstein A coefficients for the OH(3-1) band at the $\text{P}_1(2)$ and $\text{P}_1(4)$ lines as calculated by Brooke et al. (2016). The new A coefficients for the $\text{P}_1(2)$ and $\text{P}_1(4)$ lines are 9.895802 and 13.15222 s^{-1} , respectively. After correction for the A coefficients, the following equation for the OH rotational temperature estimation T_r is obtained:

$$T_r = \frac{259.58}{\ln(2.658 \cdot R)}, \quad (1)$$

where R is the brightness ratio $B(\text{P}_1(2)) / B(\text{P}_1(4))$ inferred from measurements of the $\text{P}_1(2)$ and $\text{P}_1(4)$ lines in absolute units (rayleigh). Equation (1) differs from Eq. (4) by Pautet et al. (2014) in terms of the multiplier of the R parameter: 2.658 versus 2.644. This results in a 0.7–1.2 K temperature difference between temperature estimations in the present paper and Pautet et al. (2014), for a typical range of winter temperatures (180–240 K) in the mesopause region.

3.2 Absolute calibration

The purpose of the absolute calibration of the OH imager is to establish a relationship between the arbitrary, instrument-dependent raw pixel values (counts) and the column emission rate in units of rayleigh (R). Imager absolute calibration is a multistage process that was performed by Keo Scientific Ltd. First, bandpass-filter curves for the three OH(3-1) filters (atmospheric background, the $\text{P}_1(2)$ line and $\text{P}_1(4)$ line) were measured using a tunable SWIR laser. Second, on-axis broadband sensitivity was determined by imaging the output of a calibrated National Institute of Standards and Technology (NIST)-traceable integrating sphere through the imager, including the filters, and onto the InGaAs photodiode

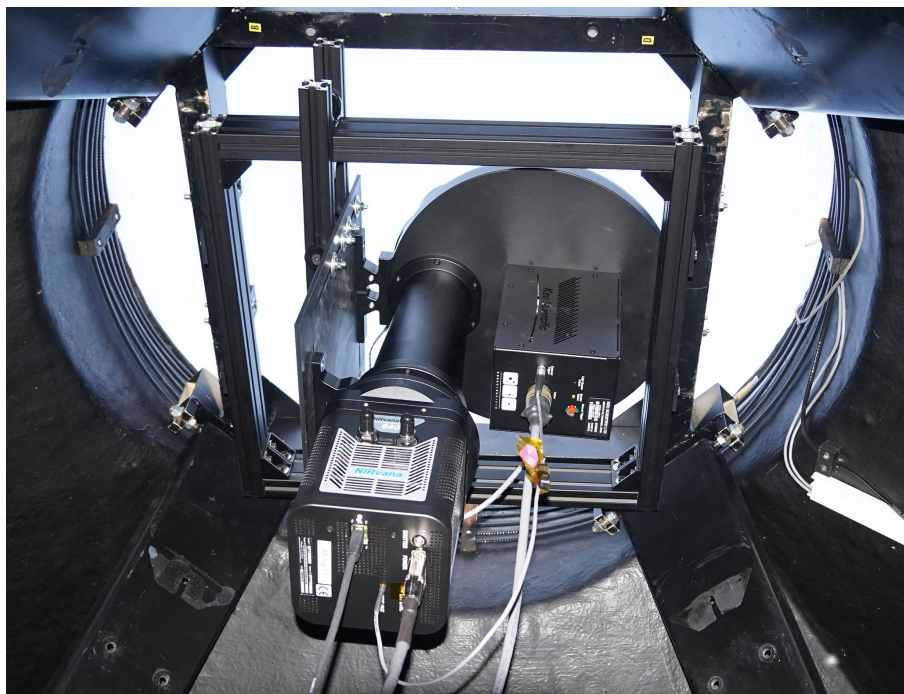


Figure 1. The Keo Scientific OH imager installed in November 2022 at the Swedish Institute of Space Physics (IRF) in Kiruna, Sweden (67.86° N, 20.42° E). The image was taken by Peter Dalin.

array sensor. Additionally, on-axis, “at-wavelength” sensitivity was measured for each filter using a collimated laser beam calibrated with a NIST-traceable optical power meter through the imager and onto the InGaAs photodiode array sensor. This resulted in the final absolute calibration coefficients, valid on-axis. Finally, a flat-field correction procedure was performed to compensate for off-axis vignetting, resulting in uniformity coefficients (one for each OH filter), allowing one to apply the absolute calibration coefficients to any pixel in the image. The flat-field correction consists of three steps: (1) the cylindrically symmetric component of the lenses is characterized first. This is done on an optical bench (180° rotary table) and an integrating sphere, where the sphere is illuminated with a tunable laser at the emission wavelengths of each of the two OH channels. (2) The imager is inserted into the integrating sphere and an additional diffuser is placed over the fisheye lens. Images are taken with the filters in place and with the uncoated glass blank in place. This is to find the attenuation of the filters relative to the uncoated glass blanks. (3) Zernike polynomials are then used for the fitting to produce the smooth flat fields. A calibration certificate with supporting files was issued by Keo Scientific.

3.3 Geometrical calibration

Geometrical calibration of the OH imager is a necessary procedure to measure the absolute horizontal coordinates of each pixel of the sensor at the instrument location. The geometrical calibration was performed by analyzing images of a clear

night sky with reference stars using a wide-band filter (1000–1600 nm) in the filter wheel. The Positions and Proper Motions (PPM) Star Catalogue was used to identify the positions of the reference stars. The third-order polynomial P describes the camera optical model:

$$P = a_1 \cdot x^3 + a_2 \cdot x^2 y + a_3 \cdot y^2 x + a_4 \cdot y^3 + a_5 \cdot x^2 + a_6 \cdot xy + a_7 \cdot y^2 + a_8 \cdot x + a_9 \cdot y + a_{10}, \quad (2)$$

where the 10 a_i parameters are free coefficients and x and y are the horizontal coordinates of the reference stars in the analyzed image. By comparing the theoretical horizontal coordinates of reference stars (more than 50 reference stars have been identified in reference images) with their measured coordinates, 10 free coefficients of the third-order polynomial were calculated using the least-squares method. These 10 coefficients describe all possible optical distortions in the whole camera optical path. This procedure finally resulted in the calculation of the absolute horizontal coordinates (elevation and azimuth angles) of each pixel, followed by a georeference procedure to project each pixel onto the Earth’s surface. For this, the mean altitudes of the OH and O₂ layers were chosen as 87 and 94 km, respectively. The spatial horizontal resolution in the center of the image is about 0.3 km, reaching ~ 1.2 km at the edges of the image.

3.4 Error analysis

In order to estimate the total error of temperature estimation, we need to rewrite the basic Eq. (1). The R brightness ratio in Eq. (1) depends on four variables represented by their raw measurement values in counts: the raw intensity of the $P_1(2)$ line I_{P12} , the raw intensity of the $P_1(4)$ line I_{P14} , the atmospheric background raw intensity I_{bg} and instrumental dark-current noise n_{dc} . The raw intensities I_{P12} and I_{P14} mean that no corrections for the atmospheric background and noise have been made. Thus, Eq. (1) can be rewritten in terms of these four variables as follows:

$$T_r = \frac{259.58}{\ln \left(2.658 \cdot \frac{k_1 \cdot k_4 \cdot (k_2 \cdot I_{P12} - k_3 \cdot I_{bg} + 0.22 \cdot n_{dc})}{k_5 \cdot k_7 \cdot (k_6 \cdot I_{P14} - k_3 \cdot I_{bg} + 0.60 \cdot n_{dc})} \right)}, \quad (3)$$

where k_1 , k_2 , k_3 , k_4 , k_5 , k_6 and k_7 are the coefficients determined in the laboratory during the absolute calibration procedure. Equation (3) comes from Eq. (1) in the following way: the R brightness ratio in Eq. (1) is in absolute units (rayleigh). The instrument registers emission intensities ($P_1(2)$, $P_1(4)$ and atmospheric background) in relative digital units (counts). In order to relate relative to absolute units, the absolute calibration is performed. The main part of this procedure is to determine the absolute filter sensitivities that are different for each filter. These are the coefficients k_2 , k_3 and k_6 in Eq. (3). In addition, the dark noise is subtracted both from the $P_1(2)$ and $P_1(4)$ lines and from the atmospheric background line, which, in turn, is finally subtracted from the $P_1(2)$ and $P_1(4)$ lines. Since the coefficients k_2 , k_3 and k_6 are different, this procedure results in different constants (0.22 and 0.60) for the subtracted dark noise in the numerator and denominator in Eq. (3). These constants have positive signs since the dark noise is subtracted from the $P_1(2)$ and $P_1(4)$ lines and from the atmospheric background line with different coefficients. The coefficients k_4 and k_7 describe the flat field-correction factors as being different for each OH(3-1) emission line. Finally, the coefficients k_1 and k_5 convert photometric units to rayleigh, including several multipliers and the geometric etendue.

In order to estimate these four raw measurement values (I_{P12} , I_{P14} , I_{bg} and n_{dc}) and their errors, we follow the method proposed by Pautet et al. (2014). Measurements should be performed during a time when atmospheric and geomagnetic perturbations are at a minimum (i.e., only small variations in raw OH emission lines and in the atmospheric background, no contamination by tropospheric clouds, and no auroral emissions). A period of 1 h on 6 April 2023 was chosen to evaluate the four raw measurement variables and their errors. Figure 2 illustrates the raw intensities for the $P_1(2)$ and $P_1(4)$ lines as well as for the raw atmospheric background (BG) measured at the zenith over a single-pixel area ($0.003 \times 0.003^\circ$). To reduce measurement perturbations as much as possible, the raw data were smoothed using a three-point moving average. Then the residuals were

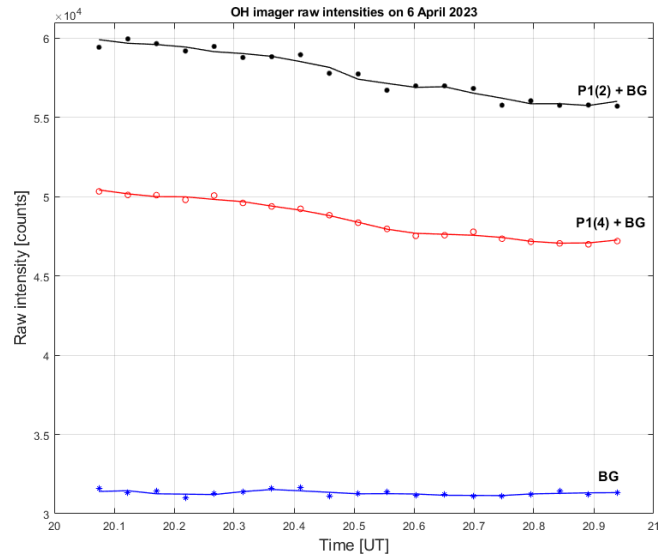


Figure 2. Raw intensities of emission lines at the zenith as measured by the OH imager in Kiruna on 6 April 2023. The black dots, red circles and blue asterisks are the raw intensities of the OH $P_1(2)$, OH $P_1(4)$ (including atmospheric background and noise level of the detector) and raw atmospheric background (BG) lines, respectively. The black, red and blue lines are three-point moving averages.

determined by subtracting the smoothed curves from the raw intensity data, and their standard deviations were estimated. We obtained the following smoothed average values and their standard deviations: $57\,711 \pm 290$ counts for the $P_1(2)$ line, $48\,552 \pm 110$ counts for the $P_1(4)$ line and $31\,301 \pm 126$ counts for the BG. The measured random temperature error (δT_m) is calculated using a general equation of error propagation in the case of a function having several variables (Taylor, 1997):

$$\delta T_m = \sqrt{\left(\frac{\partial T}{\partial I_{P12}} \delta I_{P12} \right)^2 + \left(\frac{\partial T}{\partial I_{P14}} \delta I_{P14} \right)^2 + \left(\frac{\partial T}{\partial I_{bg}} \delta I_{bg} \right)^2}, \quad (4)$$

where $\partial T / \partial I_{P12}$, $\partial T / \partial I_{P14}$ and $\partial T / \partial I_{bg}$ are the partial derivatives of T_r (see Eq. 3) with respect to raw intensity values $P_1(2)$, $P_1(4)$ and atmospheric background, respectively, and δI_{P12} , δI_{P14} and δI_{bg} are their standard deviations. When inserting the parameters that were estimated above into Eq. (4), a temperature measurement random error of 1.80 K is derived.

The temperature instrumental error is mainly governed by the dark-current noise of the CCD sensor and by the coefficients $k_{1,2,3,4,5,6,7}$ in Eq. (3). The dark-current noise was continuously monitored using the dark-blocking filter as part of the measurement cycle (every 2.75 min) and was subsequently subtracted from the recorded raw intensity values of the OH and O_2 emission lines. An example of dark-current noise is shown in Fig. 3, demonstrating the linear stability of the dark-current noise during the night of 6–7 April 2023, with a small, statistically insignificant regression co-

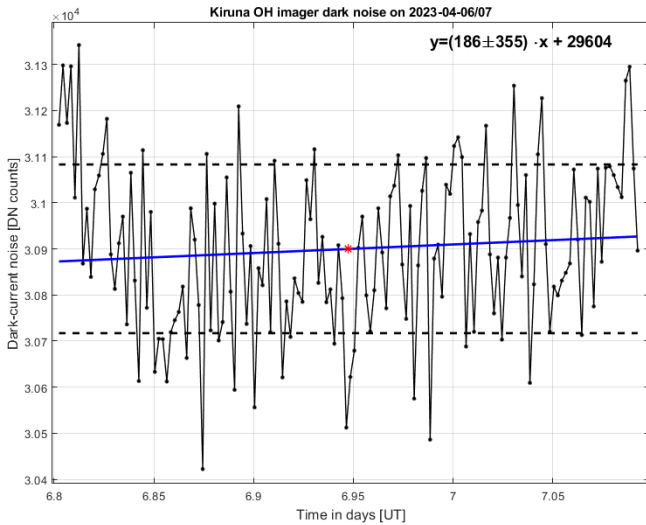


Figure 3. Example of the dark-current noise of the OH imager in Kiruna on the night of 6–7 April 2023. The black dots are dark-current noise counts in the detector center, the blue line is the linear regression, the red asterisk is the mean dark-current noise and the dashed lines are 1 standard deviation around the mean noise.

efficient equal to 186 ± 355 counts d^{-1} . The mean value of the dark-current noise n_{dc} and its standard deviation δn_{dc} is $30\,900 \pm 183$ counts for this night. The relative errors of the coefficients $k_{1,2,3,4,5,6,7}$ were estimated to vary from 0.8 % to 4.2 % in the course of the absolute calibration, which results in temperature errors ranging from 0.1 to 2.1 K.

The total (instrumental and measurement) error δT_{tot} is calculated by adding the terms for the instrumental error to Eq. (4):

$$\delta T_{\text{tot}} = \sqrt{\left(\frac{\partial T}{\partial n_{\text{dc}}} \delta n_{\text{dc}}\right)^2 + \left(\frac{\partial T}{\partial k_i} \delta k_i\right)^2 + \left(\frac{\partial T}{\partial I_{P12}} \delta I_{P12}\right)^2 + \left(\frac{\partial T}{\partial I_{P14}} \delta I_{P14}\right)^2 + \left(\frac{\partial T}{\partial I_{Bg}} \delta I_{Bg}\right)^2}, \quad (5)$$

where $\partial T / \partial n_{\text{dc}}$ and $\partial T / \partial k_{i=1,2,3,4,5,6,7}$ are partial derivatives of the temperature with respect to dark-current noise n_{dc} , and the coefficients $k_{i=1,2,3,4,5,6,7}$, δn_{dc} and $\delta k_{i=1,2,3,4,5,6,7}$ are their standard deviations. Based on the above estimated mean dark-current noise and its standard deviation, the mean temperature instrumental error due to dark-current noise is equal to 0.15 K on the night of 6–7 April 2023. The instrumental temperature error due to the coefficients $k_{1,2,3,4,5,6,7}$ is equal to 3.37 K, and the total instrumental temperature error $\left(\sqrt{(0.15^2 + 3.37^2)}\right)$ is 3.38 K. Finally, the resulting rotational temperature and its total error $\left(\sqrt{(1.80^2 + 3.38^2)}\right)$ is equal to 193.9 ± 3.8 K for the particular case shown in Fig. 2.

At the same time, we should note that the actual variability of atmospheric conditions due to complex wave dynamics (turbulence, gravity and planetary waves, solar and lunar

tides, and seasonal variations) is greater, resulting in an average standard deviation of the mesopause temperature above Kiruna of ~ 10 K in 2023 (see Sect. 5). Most important is that the OH imager enables the resolution of small temperature variations of 4–6 K due to small-scale gravity waves, as will be demonstrated in Sect. 5.

4 Temperature validation and comparison

4.1 OH imager and lidar measurements

A Rayleigh–Mie–Raman backscatter lidar located at Esrange (~ 40 km east of Kiruna) is used to validate the OH(3-1) temperatures as measured by the OH imager. The Esrange lidar was developed by Bonn University to monitor aerosols in the troposphere, stratosphere and mesosphere (Blum and Fricke, 2005). The signal from the aerosol-free part of the atmosphere can be used to determine the temperature, assuming atmospheric hydrostatic equilibrium. The vertical and time resolutions of the obtained measurements are 150 m and 4.2 min, respectively. We used a lidar backscattered signal from the 532 nm wavelength channel to calculate an atmospheric temperature profile above Esrange. Note that the temperature profile measured by the Esrange lidar is located in the field of view of the OH imager; i.e., common-volume simultaneous temperature measurements have been conducted to validate the OH(3-1) temperatures.

The Esrange lidar was operated when weather conditions were favorable during seven nights in the period from January to March 2023. An example of a temperature comparison, made on the night of 2–3 February 2023, between the OH imager and lidar is shown in Fig. 4. The OH temperature measurement has been selected from the temperature map as the one with the closest position to Esrange with 0.3 km uncertainty. At the upper end of the profile (at around 90 km), a seed temperature equal to 188 K was taken from Aura MLS satellite temperature measurements. The mean values of the OH(3-1) and lidar temperatures averaged for the time interval between 18:43 and 05:58 UTC on this night are presented. In addition, the lidar temperature profile has been smoothed using a 1.5 km running average in height in order to reduce large fluctuations in the upper part of the profile. The Aura MLS temperature profile with the closest position to Kiruna (about 420 km away) for this case is shown in Fig. 4 by the red line. Since the OH(3-1) temperature is measured across the whole OH layer between about 82 and 92 km, with a mean height of ~ 87 km, for validation purposes the lidar temperature profile has been processed using a Gaussian function with the maximum at 87 km and with the full width at half maximum (FWHM) of 9.3 km height-weighted between 82 and 90 km, the same technique as was used by Pautet et al. (2014). The average height-weighted lidar temperature is equal to 191.8 ± 12.3 K, and the average OH(3-1) temperature is 193.6 ± 8.3 K. The temperature dif-

ference between these estimations is 1.8 K for this particular night, i.e., within the error margin. Following the same technique, we have made comparisons between the OH(3-1) and lidar temperatures for all seven available nights of simultaneous common-volume measurements, resulting in the following statistic: the average temperature difference, including the sign, between the OH imager and Esrange lidar is -0.2 ± 1.6 K. It means that, from a statistical point of view, the difference between the OH(3-1) and Esrange lidar temperatures is about zero. The maximum temperature difference between these instruments was -2.9 K on the night of 5–6 March 2023. Note that we estimate the Gaussian height-weighted lidar temperature between 82 and 90 km with the mean height of 87 km. However, the actual height distribution of the OH layer above Esrange is unknown since it varies, in general, in time and space (i.e., Pautet et al., 2014). Thus, one can conclude that there is good agreement between the OH(3-1) and Esrange lidar temperature measurements on individual nights (within 3 K) and on an average basis (close to zero), after taking into account the dynamical processes in the mesopause region and instrument errors.

4.2 OH imager and Aura MLS measurements

The Microwave Limb Sounder (MLS) radiometer on board the Aura satellite provides temperature profiles of the middle atmosphere with near-global coverage. Aura MLS temperature data (V5.0 and Level 2 data quality) can be obtained from the NASA public website: https://acdisc.gesdisc.eosdis.nasa.gov/data/Aura_MLS_Level2/ (last access: 28 February 2024). The description of MLS temperature retrieval and its validation can be found in Froidevaux et al. (2006) and Schwartz et al. (2008). We used Aura MLS temperature profiles as an additional way to compare temperatures that were retrieved with the OH imager.

The vertical resolution of Aura MLS temperature measurements is about 11–12 km in the mesopause region, and temperature precision of individual profiles is about 3.5 K at mesopause heights (see the Aura MLS data quality and description document available on the NASA website). Aura MLS temperatures at the pressure level of 4.6×10^{-3} hPa (about 86 km altitude) were chosen to be closest to the OH imager location (less than 300 km from Kiruna) and were measured simultaneously with OH(3-1) temperatures within the same hour. The comparison between OH imager and Aura MLS temperature measurements for the period January–April 2023 is illustrated in Fig. 5. In total, 22 individual temperature measurements have been collected. One can see that there are several cases in which the temperatures agree well within their uncertainties (days of the year 14, 58, 61, 65, 83, 85, 86, 92, 93, 99 and 101). For other days the agreement is worse. Note that even if the Aura MLS instrument measures temperature in the closest proximity to the OH imager, the Aura MLS horizontally scans a rather large volume of the mesopause (about 250–280 km) along

its trajectory, which is not exactly the same mesopause volume as that which the OH imager measures; aside from this, the vertical resolution of Aura MLS temperature data in the mesopause is not equal to the width of the OH layer. All these factors complicate precise comparison. Natural variabilities of the atmosphere due to wave dynamics and chemical processes result in different temperatures in different atmospheric volumes. At the same time, two important conclusions can be drawn from Fig. 5: (a) there is no systematic bias (neither negative nor positive) in the OH(3-1) temperature relative to the Aura MLS temperature since there are OH(3-1) temperatures higher and lower than Aura MLS temperatures, and (b) the average temperature difference, including the sign, between the OH imager and Aura MLS is 2.8 ± 7.8 K. This is a small difference, taking into account the abovementioned limitations.

5 Results and discussion

Maps of OH(3-1) intensities in rayleigh and O₂ IR A-band intensity in relative units, as well as the OH(3-1) temperature map on 16 February 2023, are illustrated in Fig. 6. One can see there is fine modulation of the temperature (Fig. 6d) due to small-scale gravity waves with wavelengths of 4–8 km overlying larger gravity-wave crests; the temperature amplitudes due to these small-scale waves are in the range of 4–6 K. It means that this case clearly demonstrates the ability of the OH imager to resolve small-amplitude, small-scale dynamical temperature variations that are important for studying the high-frequency range of the gravity-wave spectrum. Figure 7 illustrates a zoom of the images shown by the black squares in Fig. 6, which focuses on the small-scale wave structure of the approximately 4–6 km wavelength in the P₁(2), P₁(4) and temperature maps. Residuals of the P₁(2) and P₁(4) intensities are shown after subtraction of the mean intensity values from these zoomed-in images. Note that the temperature estimation (see Eq. 1) is not a linear function of the P₁(2) and P₁(4) line intensities, meaning that the linear scale of the P₁(2) and P₁(4) changes shown in Fig. 7a and b cannot directly represent the temperature changes in the observed small-scale wave structures shown in Fig. 7d. Another important feature of this case is that there is a medium-scale modulation, oriented in the direction from northwest to southeast, with horizontal wavelengths of 20–40 km and temperature amplitudes of 7–10 K. These medium-scale gravity-wave crests are clearly seen on all four maps, meaning that the same gravity-wave package was propagating through both the OH layer (maximum at ~ 87 km) and the O₂ layer (maximum at ~ 94 km). An analysis of the sequence of temperature maps has demonstrated that these medium-scale gravity waves were moving from southwest to northeast, with an observed horizontal-phase speed of about 30–35 m s⁻¹. This type of medium-scale gravity wave is common in the mesopause region (e.g., Pautet et

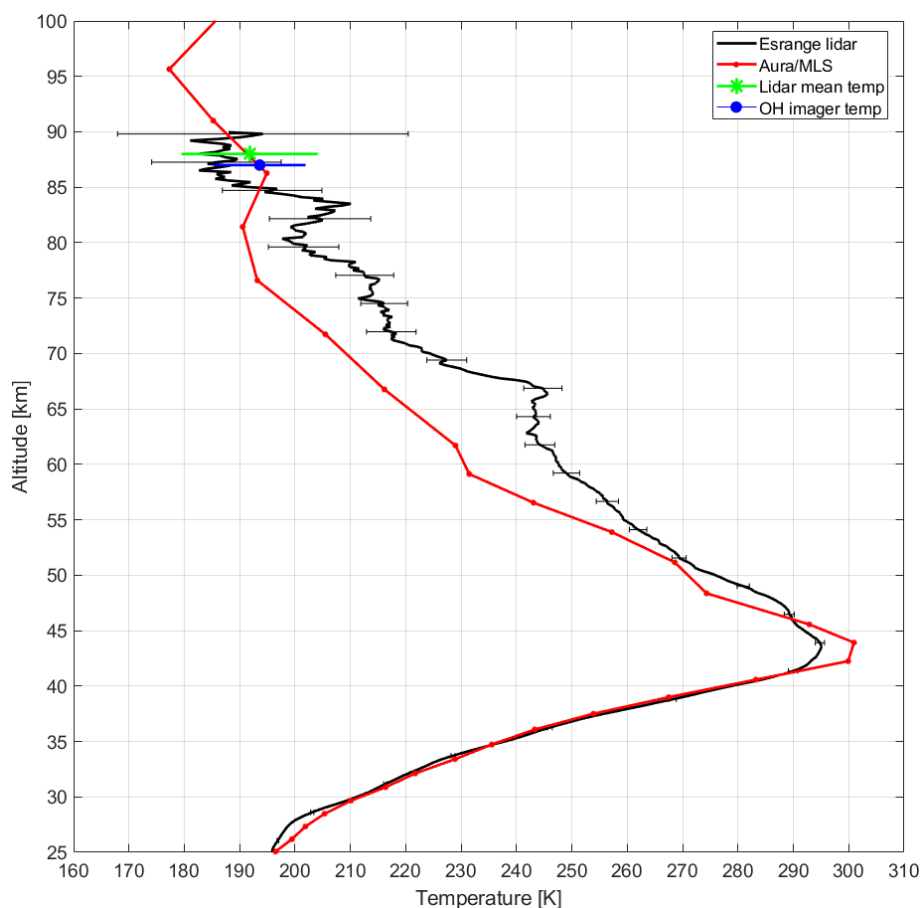


Figure 4. Temperature measurements made between 18:43 and 05:58 UTC on the night of 2–3 February 2023. The blue dot is the mean OH(3-1) temperature at 87 km averaged over the same time period. The black line is the Esrange lidar mean temperature profile. The green asterisk is the average height-weighted lidar temperature as calculated by vertical averaging across the OH layer (see text). Error bars for the OH imager and lidar measurements are 1 standard deviation of the temperature variations for the night. The red line is the Aura MLS temperature profile at 70.3° N, 12.2° E, closest to the position of Kiruna (about 420 km away), measured at 02:32 UTC on 3 February 2023.

al., 2011; Demissie et al., 2014). Thus, the OH imager allows the retrieval of information on gravity waves propagating in both horizontal and vertical domains in the mesopause region. A detailed analysis of gravity-wave characteristics and of the gravity-wave spectrum is beyond the scope of this paper and will be addressed in future studies. A file named “OH_imager_video_160223.avi”, which can be found in the Supplement to Dalin (2024) (see “Data availability”), contains a video sequence of the intensities and temperature maps shown in Fig. 6. The video demonstrates the motion of atmospheric gravity waves of various scales, moving preferentially from the southwest to the northeast.

The OH(3-1) daily mean rotational temperatures measured above Kiruna for the 2023 winter season (13 January–16 April) are illustrated by the black circles in Fig. 8. The OH(3-1) temperature values are within the range of 178–224 K. The average daily winter temperature for this particular period is equal to 203 ± 10 K. For comparison, Aura MLS temperatures close to the Kiruna location (less than 675 km

away) are indicated by the red circles. There is good agreement between these time series, with a small average temperature difference of 1.9 ± 6.9 K. The temperature behavior agrees well with the general seasonal temperature behavior in the winter mesopause, with a maximum in the period of December–February followed by a rapid temperature decrease in March–April (e.g., Perminov et al., 2018). Kim et al. (2017) have analyzed mesopause temperatures from OH airglow measurements with a Fourier-transform spectrometer (FTS) for the winter periods of 2003–2014 in Kiruna. The authors have found variations in the winter mesopause temperature above Kiruna in the range of 180–230 K. This temperature range agrees well with the OH(3-1) temperature values presented in Fig. 8. Cho et al. (2011) have studied OH and O₂ airglow temperatures for the winter periods of 2001–2007, measured with a spectral airglow temperature imager (SATI) instrument and a Michelson interferometer, at high northern latitudes at Resolute Bay and Esrange, respectively. Cho et al. (2011) have demonstrated that win-

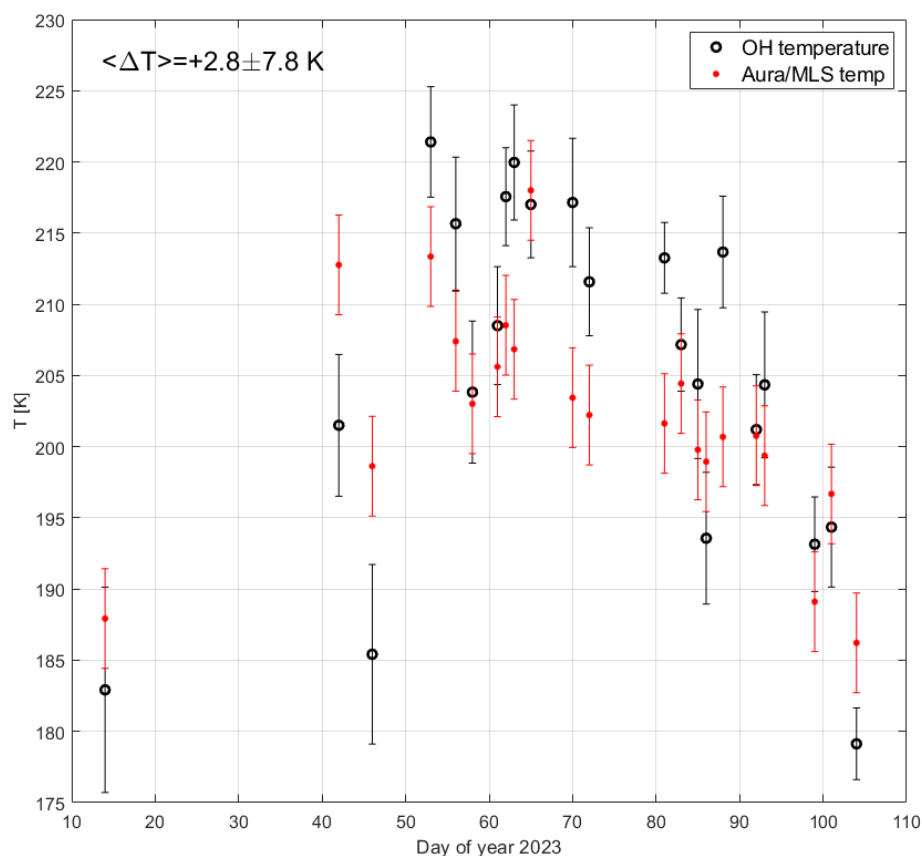


Figure 5. A comparison between simultaneous measurements of the mesopause temperature performed by the OH imager (black circles) above Kiruna at ~ 87 km and by Aura MLS (red points) at 0.0046 hPa (~ 86 km), close to the Kiruna location (distance difference is less than 300 km). Error bars of the OH(3-1) temperature are 1 standard deviation for a particular hour. Error bars of the Aura MLS temperature are equal to 3.5 K (see text).

ter mesopause temperatures vary between 180 and 245 K, which again agrees well with the temperature range obtained by the OH imager. Sigernes et al. (2003) have studied daily mesospheric winter temperatures for more than 20 years of ground-based spectral measurements of the OH layer over Svalbard from 1980 to 2001. The authors have found the average daily winter temperature to be equal to 208 ± 15 K, with a maximum and minimum temperature of 257 and 168 K, respectively, emphasizing that the mesospheric temperature variations over Svalbard in winter are extremely high. The average daily winter OH(3-1) temperature that was estimated in the present study is close to the value found by Sigernes et al. (2003), taking into account the large temperature deviations of the average daily values found in both papers.

It is interesting to discuss the following feature of the OH(3-1) temperature behavior: we observed two rather strong temperature enhancements on day 52 (21 February 2023) and on day 66 (7 March 2023). The 2023 sudden stratospheric warming (SSW) event started around 1 February 2023 (<https://www.climate.gov/news-features/event-tracker/disrupted-polar-vortex-brings-sudden-stratospheric->

warming-february, last access: 29 February 2024). SSWs are accompanied by both cooling and warming of the mesopause region: cooling is observed at the time of an SSW onset or a few days later, while warming is observed with a delay of about 20–25 d (Cho et al., 2004; Shepherd et al., 2014). Sometimes several mesopause warmings (wavy oscillations) can be generated after an SSW onset (see Fig. 1b, f in Shepherd et al., 2014). This is exactly what was observed in the OH(3-1) temperature behavior: first, there was an OH(3-1) temperature decrease between days 32 and 36 (close to the 2023 SSW onset), and then the two strong temperature maxima occurred on days 52 and 66, i.e., about 20 and 34 d after the 2023 SSW onset. A detailed link of the OH(3-1) temperature above Kiruna to SSW events will be investigated in future papers.

The two emission layers (OH and O₂) are varied in space and time, making different height distances between these layers. This complicates an analysis dealing with the vertical propagation of gravity waves. At the same time, if the same wave package with the same horizontal wavelength, observed phase velocity and propagation direction is observed in both the OH and O₂ layers, one can assume that the same

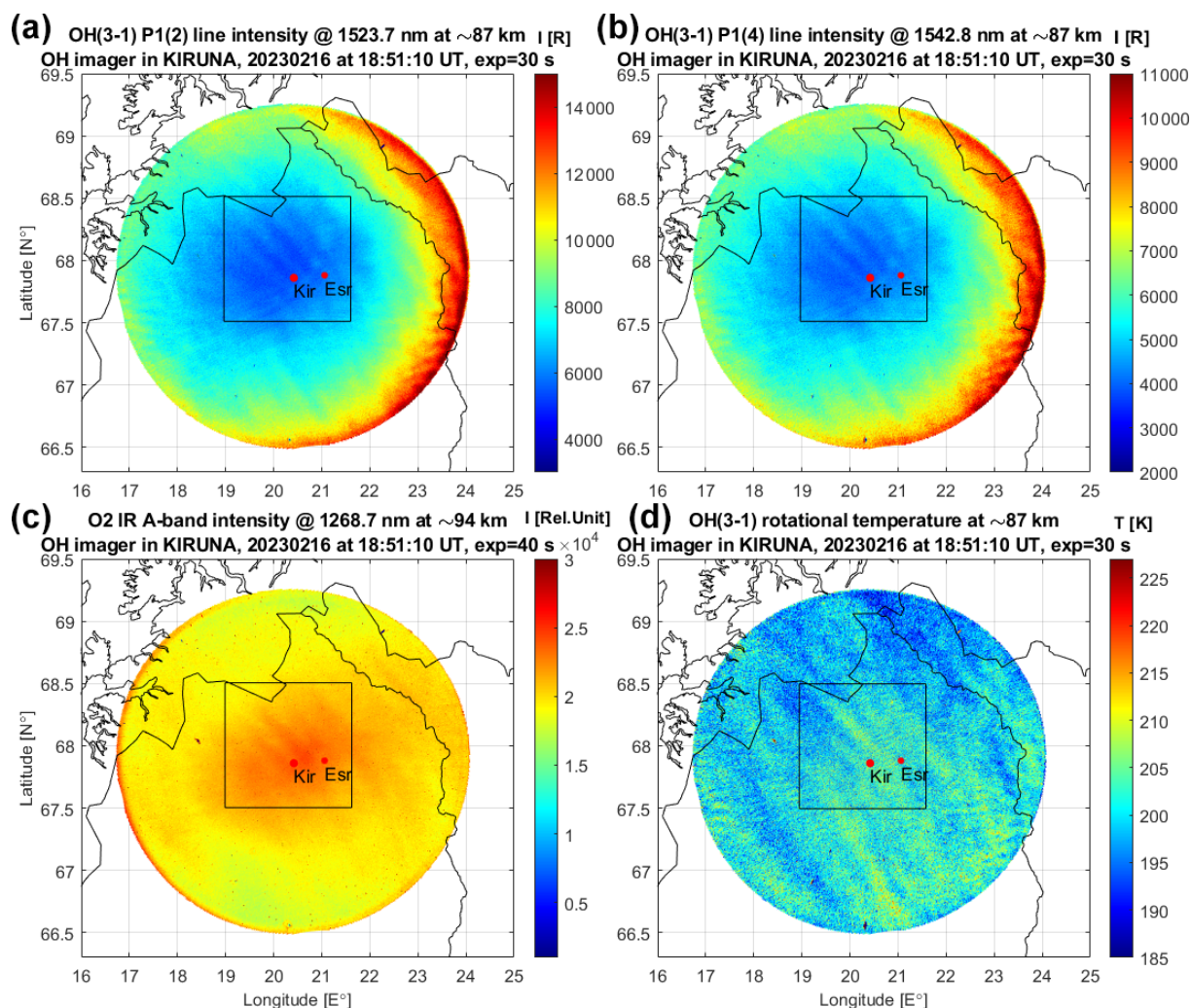


Figure 6. Maps of airglow intensities and temperature obtained from the OH imager on 16 February 2023. **(a)** Intensity in the rayleigh of the OH(3-1) P₁(2) line at 1523.7 nm. **(b)** Intensity in the rayleigh of the OH(3-1) P₁(4) line at 1542.8 nm. **(c)** Intensity in relative units of the O₂ IR A-band at 1268.7 nm. **(d)** OH(3-1) rotational temperature estimated using the brightness ratio of the two OH(3-1) emission lines (see text). The timestamp in all the maps corresponds to the time of the middle point of the current filter wheel cycle, which takes 2.75 min. The black squares show a zoom of the images, which is shown in Fig. 7.

gravity wave was propagating in both the horizontal and vertical domains. According to the general theory of gravity waves (e.g., Gossard and Hook, 1975), a gravity wave propagates at an angle relative to the vertical, with tilted phase lines. This should result in an observed phase shift of the same gravity wave between the OH and O₂ layers. Once a phase shift and a horizontal wavelength are estimated from the OH and O₂ maps, one can calculate the vertical wavelength using the following relation:

$$\lambda_z = \lambda_x / \tan(\alpha), \quad (6)$$

where λ_z and λ_x are the vertical and horizontal wavelengths of a gravity wave and α is the angle between wave phase lines and the vertical. Furthermore, if the buoyancy frequency N is a known quantity or is estimated using lidar or satellite

temperature profiles, one can deduce the intrinsic frequency ω of a gravity wave from the following relation:

$$\omega = \pm N \cdot \cos(\alpha). \quad (7)$$

By substituting known values of ω , N and λ_x into the dispersion relation for gravity waves, one can estimate the vertical wavelength again, thus verifying the first estimation of the vertical wavelength. Note that this method is valid for a limited number of gravity waves with vertical wavelengths less than the height distance between the two layers (about 7 km).

Another simple method to estimate the vertical wavelength of a gravity wave is based on the assumption that the height difference D between the two layers is a known quantity (Fagundes et al., 1995; Schmidt et al., 2018). If a horizontal phase shift $\Delta\varphi$ of a given wave package between both layers

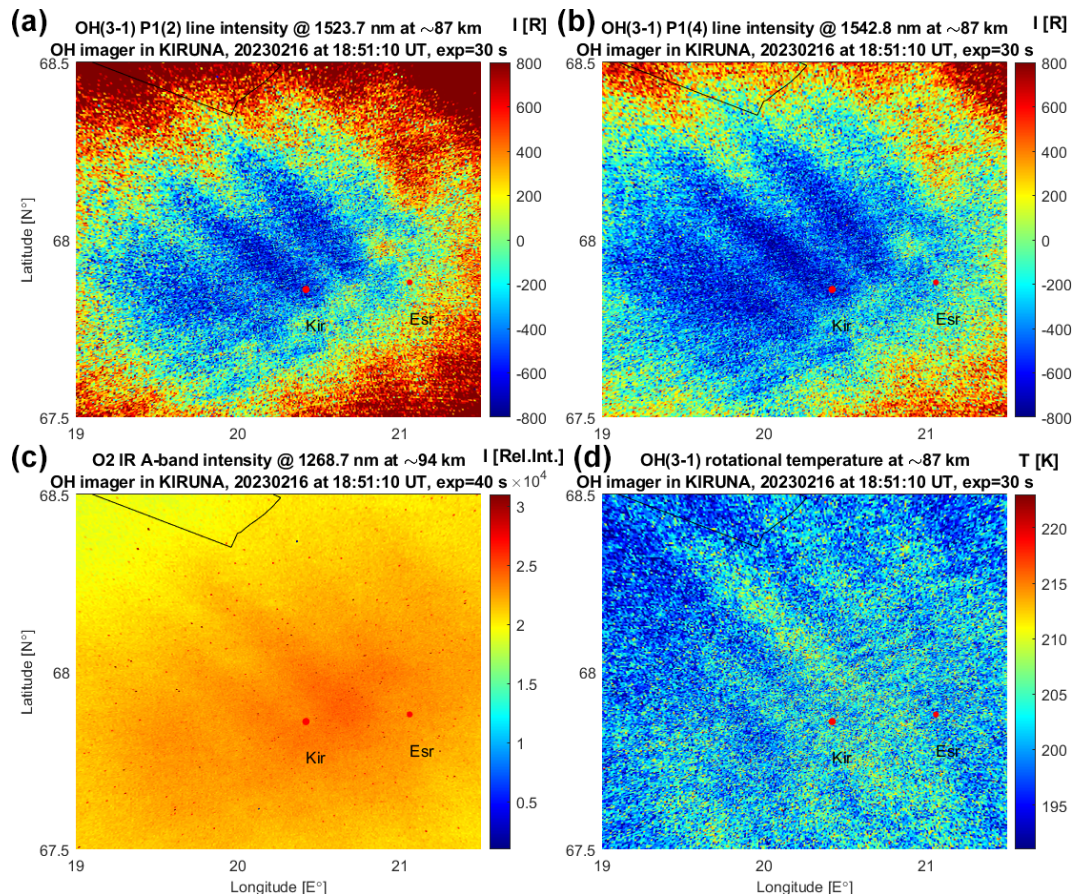


Figure 7. A zoom of the images shown in the black squares in Fig. 6, which focus on the small-scale wave structure of about 4–6 km wavelengths in (a) the P₁(2) map, (b) the P₁(4) map, (c) intensity in relative units of the O₂ IR A-band at 1268.7 nm, and (d) the temperature map. Residuals of the P₁(2) and P₁(4) intensities are shown after subtraction of the mean intensity values from these zoomed-in images.

is estimated, then one can calculate its vertical wavelength λ_z using the following relation:

$$\lambda_z = D \cdot 2\pi / \Delta\varphi. \quad (8)$$

We will use both approaches to estimate vertical wavelengths of gravity waves propagating through the OH and O₂ layers in a future paper, which will be supported by model studies of gravity waves propagating through the whole atmosphere up to the mesopause level (Dalin et al., 2015, 2016).

6 Conclusions

A novel infrared imager (OH imager) began operating in November 2022 in Kiruna (northern Sweden), aimed at studying nightglow emissions coming from the hydroxyl and molecular oxygen layers in the mesopause region. The OH imager registers selected emission lines (1523 and 1542 nm) in the OH(3-1) band to obtain emission intensity and temperature maps at around 87 km altitude. In addition, the imager records infrared emissions coming from the O₂ IR A-band

airglow at 1269 nm in order to obtain O₂ emission intensity maps at a slightly higher altitude of ~ 94 km. This technique allows for the tracing of gravity-wave disturbances in both the horizontal and vertical domains in the mesopause region. The lee location of the OH imager favors studies of mountain waves and their probable influence on the mesopause temperature and dynamics.

Temperature maps demonstrate the ability of the OH imager to resolve small-scale (4–8 km), small-amplitude (4–6 K) gravity waves as well as medium-scale gravity waves with horizontal wavelengths of 20–40 km and temperature amplitudes of 7–10 K. Such medium-scale waves have propagated through both the OH and O₂ layers.

The comparison between the OH imager and collocated Esrange lidar shows good agreement between OH(3-1) and Esrange lidar temperature measurements on individual nights (within 3 K) and on an average basis (-0.2 ± 1.6 K). The comparison between the OH imager and Aura MLS radiometer demonstrates no systematic temperature bias between these instruments and a small average temperature difference of 2.8 ± 7.8 K, which is likely caused by the variable state of

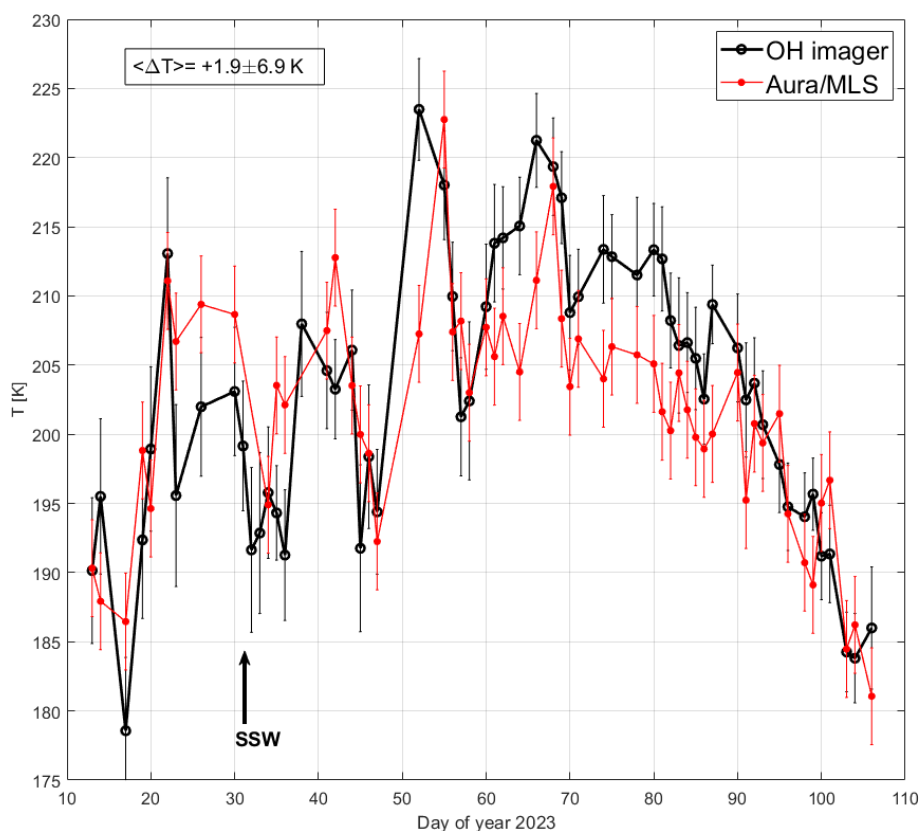


Figure 8. Daily mean OH(3-1) rotational temperature above Kiruna, at zenith, at ~ 87 km for the 2023 winter season (black circles). Aura MLS instantaneous temperature measurements close to the Kiruna location at ~ 86 km (red points). Error bars of the OH(3-1) temperature are 1 standard deviation for a particular night. Error bars of the Aura MLS temperature are equal to 3.5 K (see text). The onset of the sudden stratospheric warming is marked by the black arrow. The period considered is from 13 January to 16 April 2023.

the mesopause temperature over the spatial scales of their different observational volumes.

OH(3-1) daily mean rotational temperatures measured above Kiruna for the 2023 winter season (January–April) demonstrate typical seasonal variations, with a maximum in February and a rapid temperature decrease in April in the winter polar mesopause. The OH(3-1) temperature values are within the range of 178–224 K, which agrees well with other high-latitude temperature measurements in the winter mesopause. The average daily winter temperature for the period considered is 203 ± 10 K.

Code availability. The MATLAB code used in this study for the OH image processing is available upon request from the corresponding author (pdalin@irf.se).

Data availability. Processed OH image data from the paper's figures are available via the Swedish National Data Service at <https://doi.org/10.5878/cn8x-d486> (Dalin, 2024). Underlying research data are available upon request from Peter Dalin (pdalin@irf.se). Once the commissioning period of the OH im-

ager instrument is completed, registrations will be made freely available for noncommercial scientific usage, in accordance with other data obtained from the Kiruna Atmospheric and Geophysical Observatory (KAGO) at the Swedish Institute of Space Physics (IRF). Aura MLS temperature data (V5.0 and Level 2 data quality) can be obtained from the NASA public website after registration at https://disc.gsfc.nasa.gov/datacollection/ML2T_NRT_005.html (EOS MLS Science Team, 2022). Esrange lidar data can be made available upon request from Peter Dalin (pdalin@irf.se) or Jonas Hedin (jhedi@misu.su.se).

Author contributions. PD: conceptualization, methodology, installation of the OH imager, data processing and validation, MATLAB and Python code, statistical analysis, data visualization and archiving, geometrical calibration, and writing the original manuscript. UB: conceptualization, writing the proposal to the Swedish Research Council (Vetenskapsrådet), installation of the OH imager and providing data storage. JK: conceptualization and writing the proposal to the Swedish Research Council (Vetenskapsrådet). PV: installation of the OH imager, software development and lidar operation. TN: conceptualization, installation of the OH imager and writing Python code. TT, DW and CU: methodology, design, manufacturing and absolute calibration of the OH imager. VP and NP:

conceptualization, methodology and assistance with the interpretation of scientific results. JH: ESRANGE lidar preparation and operation. All co-authors contributed to writing and reviewing the paper.

Competing interests. The contact author has declared that none of the authors has any competing interests.

Disclaimer. Publisher's note: Copernicus Publications remains neutral with regard to jurisdictional claims made in the text, published maps, institutional affiliations, or any other geographical representation in this paper. While Copernicus Publications makes every effort to include appropriate place names, the final responsibility lies with the authors.

Acknowledgements. We are thankful to Daria Mikhaylova and Martin Rönnfalk (IRF Kiruna) for their help with the installation of the OH imager. The Aura MLS temperature data used in this effort were acquired as part of the activities of NASA's Science Mission Directorate and are archived and distributed by the Goddard Earth Sciences (GES) Data and Information Services Center (DISC).

Financial support. The OH imager installation was financed and performed as part of the research infrastructure grant no. 2021-00360 from the Swedish Research Council (Vetenskapsrådet) to the Kiruna Atmospheric and Geophysical Observatory (KAGO) at the Swedish Institute of Space Physics (IRF).

Review statement. This paper was edited by Christian von Savigny and reviewed by two anonymous referees.

References

- Ammosov, P., Gavril'yeva, G., Ammosova, A., and Koltovskoi, I.: Response of the mesopause temperatures to solar activity over Yakutia in 1999–2013, *Adv. Space Res.*, 54, 2518–2524, <https://doi.org/10.1016/j.asr.2014.06.007>, 2014.
- Baker, D. J. and Stair, A. T.: Rocket measurements of the altitude distributions of the hydroxyl airglow, *Phys. Scripta*, 37, 611–622, <https://doi.org/10.1088/0031-8949/37/4/021>, 1988.
- Bates, D. R. and Nicolet, M.: The photochemistry of atmospheric water vapour, *J. Geophys. Res.*, 55, 301–327, <https://doi.org/10.1029/JZ055i003p00301>, 1950.
- Blum, U. and Fricke, K. H.: The Bonn University lidar at the ESRANGE: technical description and capabilities for atmospheric research, *Ann. Geophys.*, 23, 1645–1658, <https://doi.org/10.5194/angeo-23-1645-2005>, 2005.
- Brooke, J. S. A., Bernath, P. F., Western, C. M., Sneden, C., Afşar, M., Li, G., and Gordon, I. E.: Line strengths of rovibrational and rotational transitions in the $X^2\Pi$ ground state of OH, *J. Quant. Spectrosc. Ra.*, 168, 142–157, <https://doi.org/10.1016/j.jqsrt.2015.07.021>, 2016.
- Chamberlain, J. W.: Physics of the aurora and airglow, 1st edn., International Geophysics Series, Academic Press, 2, 722, ISBN: 9781483222530, 1961.
- Cho, Y.-M., Shepherd, G. G., Won, Y.-I., Sargoytchev, S., Brown, S., and Solheim, B.: MLT cooling during stratospheric warming events, *Geophys. Res. Lett.*, 31, L10104, <https://doi.org/10.1029/2004GL019552>, 2004.
- Cho, Y.-M., Shepherd, G. G., Shepherd, M. G., Hocking, W. K., Mitchell, N. J., and Won, Y.-I.: A study of temperature and meridional wind relationships at high northern latitudes, *J. Atmos. Sol.-Terr. Phys.*, 73, 936–943, <https://doi.org/10.1016/j.jastp.2010.08.011>, 2011.
- Christensen, A. B., Rees, M. H., Romick, G. J., and Sivjee, G. G.: OI (7774 Å) and OI (8446 Å) emissions in aurora, *J. Geophys. Res.-Space*, 83, 1421–1425, <https://doi.org/10.1029/JA083iA04p01421>, 1978.
- Dalin, P.: Data for a novel infrared imager for studies of hydroxyl and oxygen emissions in the mesopause above northern Scandinavia, Version 1, Swedish Institute of Space Physics [data set], <https://doi.org/10.5878/cn8x-d486>, 2024.
- Dalin, P., Pogoreltsev, A., Pertsev, N., Perminov, V., Shevchuk, N., Dubietis, A., Zalcik, M., Kulikov, S., Zadorozhny, A., Kudabayeva, D., Solodovnik, A., Salakhutdinov, G., and Grigoryeva, I.: Evidence of the formation of noctilucent clouds due to propagation of an isolated gravity wave caused by a tropospheric occluded front, *Geophys. Res. Lett.*, 42, 2037–2046, <https://doi.org/10.1002/2014GL062776>, 2015.
- Dalin, P., Gavrilov, N., Pertsev, N., Perminov, V., Pogoreltsev, A., Shevchuk, N., Dubietis, A., Völger, P., Zalcik, M., Ling, A., Kulikov, S., Zadorozhny, A., Salakhutdinov, G., and Grigoryeva, I.: A case study of long gravity wave crests in noctilucent clouds and their origin in the upper tropospheric jet stream, *J. Geophys. Res.-Atmos.*, 121, 14102–14116, <https://doi.org/10.1002/2016JD025422>, 2016.
- Dalin, P., Perminov, V., Pertsev, N., and Romejko, V.: Updated long-term trends in mesopause temperature, airglow emissions, and noctilucent clouds, *J. Geophys. Res.-Atmos.*, 125, e2019JD030814, <https://doi.org/10.1029/2019JD030814>, 2020.
- Demissie, T. D., Espy, P. J., Kleinknecht, N. H., Hatlen, M., Kaifler, N., and Baumgarten, G.: Characteristics and sources of gravity waves observed in noctilucent cloud over Norway, *Atmos. Chem. Phys.*, 14, 12133–12142, <https://doi.org/10.5194/acp-14-12133-2014>, 2014.
- Dessler, A. E., Zhang, Z., and Yang, P.: Water-vapor climate feedback inferred from climate fluctuations, 2003–2008, *Geophys. Res. Lett.*, 35, L20704, <https://doi.org/10.1029/2008GL035333>, 2008.
- EOS MLS Science Team: MLS/Aura Near-Real-Time L2 Temperature V005, Greenbelt, MD, USA, Goddard Earth Sciences Data and Information Services Center (GES DISC), https://disc.gsfc.nasa.gov/datacollection/ML2T_NRT_005.html (last access: 1 March 2024), 2022.
- Espy, P. J. and Stegman, J.: Trends and variability of mesospheric temperature at high latitudes, *Phys. Chem. Earth*, 27, 543–553, [https://doi.org/10.1016/S1474-7065\(02\)00036-0](https://doi.org/10.1016/S1474-7065(02)00036-0), 2002.
- Fagundes, P. R., Takahashi, H., Sahai, Y., and Gobbi, D.: Observations of gravity waves from multispectral mesospheric nightglow emissions observed at 23° S, *J. Atmos. Terr. Phys.*, 57, 395–405, [https://doi.org/10.1016/0021-9169\(94\)E0007-A](https://doi.org/10.1016/0021-9169(94)E0007-A), 1995.

- French, W. J. R., Mulligan, F. J., and Klekociuk, A. R.: Analysis of 24 years of mesopause region OH rotational temperature observations at Davis, Antarctica – Part 1: long-term trends, *Atmos. Chem. Phys.*, 20, 6379–6394, <https://doi.org/10.5194/acp-20-6379-2020>, 2020.
- Fritts, D. C. and Alexander, M. J.: Gravity wave dynamics and effects in the middle atmosphere, *Rev. Geophys.*, 41, 1003, <https://doi.org/10.1029/2001RG000106>, 2003.
- Froidevaux, L., Livesey, N. J., Read, W. G., Jiang, Y. B., Jiménez, C. C., Filipiak, M. J., Schwartz, M. J., Santee, M. L., Pumphrey, H. C., Jiang, J. H., Wu, D. L., Manney, G. L., Drouin, B. J., Waters, J. W., Fetzer, E. J., Bernath, P. F., Boone, C. D., Walker, K. A., Jucks, K. W., Toon, G. C., Margitan, J. J., Sen, B., Webster, C. R., Christensen, L. E., Elkins, J. W., Atlas, E., Lueb, R. A., and Hendershot, R.: Early validation analyses of atmospheric profiles from EOS MLS on the Aura satellite, *IEEE T. Geosci. Remote*, 44, 1106–1121, 2006.
- Gao, H., Xu, J. Y., Chen, G. M., Yuan, W., and Beletsky, A. B.: Global distributions of OH and O₂ (1.27 μm) nightglow emissions observed by TIMED satellite, *Sci. China Technol. Sc.*, 54, 447–456, <https://doi.org/10.1007/s11431-010-4236-5>, 2011.
- Garcia, F. J., Taylor, M. J., and Kelley, M. C.: Two-dimensional spectral analysis of mesospheric airglow image data, *Appl. Optics*, 36, 7374–7385, <https://doi.org/10.1364/AO.36.007374>, 1997.
- Gavrilov, N., Popov, A., Dalin, P., Perminov, V., Pertsev, N., Medvedeva, I., Ammosov, P., Gavrilieva, G., and Koltovskoi, I.: Multiyear variations of time-correlated mesoscale OH temperature perturbations near the mesopause at Maymaga, Tory and Zvenigorod, *Adv. Space Res.*, 73, 3408–3422, <https://doi.org/10.1016/j.asr.2023.05.049>, 2024.
- Gossard, E. E. and Hook, W. H.: *Waves in the atmosphere*, Elsevier Scientific Publishing Company, Amsterdam, 532 pp., ISBN 978-0444411969, 1975.
- Grygalashvily, M., Sonnemann, G. R., Lübken, F.-J., Hartogh, P., and Berger, U.: Hydroxyl layer: mean state and trends at midlatitudes, *J. Geophys. Res.-Atmos.*, 119, 12391–12419, <https://doi.org/10.1002/2014JD022094>, 2014.
- Hannawald, P., Schmidt, C., Wüst, S., and Bittner, M.: A fast SWIR imager for observations of transient features in OH airglow, *Atmos. Meas. Tech.*, 9, 1461–1472, <https://doi.org/10.5194/amt-9-1461-2016>, 2016.
- Hecht, J. H., Liu, A. Z., Fritts, D. C., Walterscheid, R. L., Gelinas, L. J., and Rudy, R. J.: A “boreing” night of observations of the upper mesosphere and lower thermosphere over the Andes Lidar Observatory, *J. Geophys. Res.-Atmos.*, 128, e2023JD038754, <https://doi.org/10.1029/2023JD038754>, 2023.
- Kalicsky, C., Knieling, P., Koppmann, R., Offermann, D., Steinbrecht, W., and Wintel, J.: Long-term dynamics of OH* temperatures over central Europe: trends and solar correlations, *Atmos. Chem. Phys.*, 16, 15033–15047, <https://doi.org/10.5194/acp-16-15033-2016>, 2016.
- Khomich, V. Yu., Semenov, A. I., and Shefov, N. N.: *Airglow as an indicator of upper atmospheric structure and dynamics*, Springer-Verlag, Berlin, Heidelberg, <https://doi.org/10.1007/978-3-540-75833-4>, 2008.
- Kim, G., Kim, J.-H., Kim, Y. H., and Lee, Y. S.: Long-term trend of mesospheric temperatures over Kiruna (68° N, 21° E) during 2003–2014, *J. Atmos. Sol.-Terr. Phys.*, 161, 83–87, <https://doi.org/10.1016/j.jastp.2017.06.018>, 2017.
- Li, Q., Yusupov, K., Akchurin, A., Yuan, W., Liu, X., and Xu, J.: First OH airglow observation of mesospheric gravity waves over European Russia region, *J. Geophys. Res.-Space*, 123, 2168–2180, <https://doi.org/10.1002/2017JA025081>, 2018.
- Lübken, F.-J., Berger, U., and Baumgarten, G.: On the anthropogenic impact on long-term evolution of noctilucent clouds, *Geophys. Res. Lett.*, 45, 6681–6689, <https://doi.org/10.1029/2018GL077719>, 2018.
- Makhlouf, U. B., Picard, R. H., and Winick, J. R.: Photochemical-dynamical modeling of the measured response of airglow to gravity waves: 1. Basic model for OH airglow, *J. Geophys. Res.*, 100, 11289–11311, <https://doi.org/10.1029/94JD03327>, 1995.
- Mlynczak, M. G., Hunt, L. A., Garcia, R. R., Harvey, V. L., Marshall, B. T., Yue, J., Mertens, C. J., and Russell, J. M.: Cooling and contraction of the mesosphere and lower thermosphere from 2002 to 2021, *J. Geophys. Res.-Atmos.*, 127, e2022JD036767, <https://doi.org/10.1029/2022JD036767>, 2022.
- Melo, S. M. L., Lowe, R. P., and Russell, J. P.: Double-peaked hydroxyl airglow profiles observed from WINDII/UARS, *J. Geophys. Res.*, 105, 12397–12403, <https://doi.org/10.1029/1999JD901169>, 2000.
- Nishiyama, T., Taguchi, M., Suzuki, H., Dalin, P., Ogawa, Y., Brändström, U., and Sakanoi, T.: Temporal evolutions of N₂⁺ Meinel (1,2) band near 1.5 μm associated with aurora breakup and their effects on mesopause temperature estimations from OH Meinel (3,1) band, *Earth Planets Space*, 73, 30, <https://doi.org/10.1186/s40623-021-01360-0>, 2021.
- Nishiyama, T., Kagitani, M., Furutachi, S., Iwasa, Y., Ogawa, Y., Tsuda, T. T., Dalin, P., Tsuchiya, F., Nozawa, S., and Sigernes, F.: The first simultaneous spectroscopic and monochromatic imaging observations of short-wavelength infrared aurora of N₂⁺ Meinel (0,0) band at 1.1 μm with incoherent scatter radar, *Earth Planets Space*, 76, 30, <https://doi.org/10.1186/s40623-024-01969-x>, 2024.
- Offermann, D., Gusev, O., Donner, M., Forbes, J. M., Hagan, M., Mlynczak, M. G., Oberheide, J., Preusse, P., Schmidt, H., and Russell III, J. M.: Relative intensities of middle atmosphere waves, *J. Geophys. Res.*, 114, D06110, <https://doi.org/10.1029/2008JD010662>, 2009.
- Offermann, D., Hoffmann, P., Knieling, P., Koppmann, R., Oberheide, J., and Steinbrecht, W.: Long-term trend and solar cycle variations of mesospheric temperature and dynamics, *J. Geophys. Res.*, 115, D18127, <https://doi.org/10.1029/2009JD013363>, 2010.
- Pautet, P.-D., Taylor, M. J., Liu, A. Z., and Swenson, G. R.: Climatology of short-period gravity waves observed over northern Australia during the Darwin area wave experiment (DAWEX) and their dominant source regions, *J. Geophys. Res.*, 110, D03S90, <https://doi.org/10.1029/2004JD004954>, 2005.
- Pautet, P.-D., Stegman, J., Wrasse, C. M., Nielsen, K., Takahashi, H., Taylor, M. J., Hoppel, K. W., and Eckermann, S. D.: Analysis of gravity waves structures visible in noctilucent cloud images, *J. Atmos. Sol.-Terr. Phys.*, 73, 2082–2090, <https://doi.org/10.1016/j.jastp.2010.06.001>, 2011.
- Pautet, P.-D., Taylor, M. J., Pendleton, W. R., Zhao Jr., Y., Yuan, T., Esplin, R., and McLain, D.: Advanced mesospheric temperature

- mapper for high-latitude airglow studies, *Appl. Optics*, 53, 5934–5943, <https://doi.org/10.1364/AO.53.005934>, 2014.
- Perminov, V. I., Lowe, R. P., and Pertsev, N. N.: Longitudinal variations in the hydroxyl nightglow, *Adv. Space Res.*, 24, 1609–1612, [https://doi.org/10.1016/S0273-1177\(99\)00887-X](https://doi.org/10.1016/S0273-1177(99)00887-X), 1999.
- Perminov, V. I., Semenov, A. I., Pertsev, N. N., Medvedeva, I. V., Dalin, P. A., and Sukhodoev, V. A.: Multi-year behaviour of the midnight OH* temperature according to observations at Zvenigorod over 2000–2016, *Adv. Space Res.*, 61, 1901–1908, <https://doi.org/10.1016/j.asr.2017.07.020>, 2018.
- Pertsev, N. and Perminov, V.: Response of the mesopause airglow to solar activity inferred from measurements at Zvenigorod, Russia, *Ann. Geophys.*, 26, 1049–1056, <https://doi.org/10.5194/angeo-26-1049-2008>, 2008.
- Pertsev, N. N., Dalin, P. A., and Perminov, V. I.: Lunar tides in the mesopause region obtained from summer temperature of the hydroxyl emission layer, *Geomagn. Aeron.*, 61, 259–265, <https://doi.org/10.1134/S0016793221020109>, 2021.
- Plougonven, R. and Zhang, F.: Internal gravity waves from atmospheric jets and fronts, *Rev. Geophys.*, 52, 33–76, <https://doi.org/10.1002/2012RG000419>, 2014.
- Reid, I. M., Spargo, A. J., and Woithe, J. M.: Seasonal variations of the nighttime O(1S) and OH(8-3) airglow intensity at Adelaide, Australia, *J. Geophys. Res.-Atmos.*, 119, 6991–7013, <https://doi.org/10.1002/2013JD020906>, 2014.
- Roble, R. G. and Dickinson, R. E.: How will changes in carbon dioxide and methane modify the mean structure of the mesosphere and thermosphere?, *Geophys. Res. Lett.*, 16, 1441–1444, <https://doi.org/10.1029/GL016i012p01441>, 1989.
- Savigny, C.: Airglow in the Earth atmosphere: basic characteristics and excitation mechanisms, *ChemTexts*, 3, 14, <https://doi.org/10.1007/s40828-017-0051-y>, 2017.
- Schmidt, C., Höppner, K., and Bittner, M.: A ground-based spectrometer equipped with an InGaAs array for routine observations of OH(3-1) rotational temperatures in the mesopause region, *J. Atmos. Sol.-Terr. Phys.*, 102, 125–139, <https://doi.org/10.1016/j.jastp.2013.05.001>, 2013.
- Schmidt, C., Dunker, T., Lichtenstern, S., Scheer, J., Wüst, S., Hoppe, U.-P., and Bittner, M.: Derivation of vertical wavelengths of gravity waves in the MLT-region from multispectral airglow observations, *J. Atmos. Sol.-Terr. Phys.*, 173, 119–127, <https://doi.org/10.1016/j.jastp.2018.03.002>, 2018.
- Schwartz, M. J., Lambert, A., Manney, G. L., Read, W. G., Livesey, N. J., Froidevaux, L., Ao, C. O., Bernath, P. F., Boone, C. D., Cofield, R. E., Daffer, W. H., Drouin, B. J., Fetzer, E. J., Fuller, R. A., Jarnot, R. F., Jiang, J. H., Jiang, Y. B., Knosp, B. W., Krüger, K., Li, J.-L. F., Mlynchak, M. G., Pawson, S., Russell III, J. M., Santee, M. L., Snyder, W. V., Stek, P. C., Thurstans, R. P., Tompkins, A. M., Wagner, P. A., Walker, K. A., Waters, J. W., and Wu, D. L.: Validation of the Aura Microwave Limb Sounder temperature and geopotential height measurements, *J. Geophys. Res.*, 113, D15S11, <https://doi.org/10.1029/2007JD008783>, 2008.
- Semenov, A. I. and Shefov, N. N.: Empirical model of hydroxyl emission variations, *Int. J. Geomagn. Aeron.*, 1, 229–242, <https://doi.org/10.1134/S0016793207010161>, 1999.
- Shepherd, M. G., Beagley, S. R., and Fomichev, V. I.: Stratospheric warming influence on the mesosphere/lower thermosphere as seen by the extended CMAM, *Ann. Geophys.*, 32, 589–608, <https://doi.org/10.5194/angeo-32-589-2014>, 2014.
- Sigernes, F., Shumilov, N., Deehr, C. S., Nielsen, K. P., Svenøe, T., and Havnes, O.: Hydroxyl rotational temperature record from the auroral station in Adventdalen, Svalbard (78° N, 15° E), *J. Geophys. Res.*, 108, 1342, <https://doi.org/10.1029/2001JA009023>, 2003.
- Sivjee, G. G. and Hamwey, R. M.: Temperature and chemistry of the polar mesopause OH, *J. Geophys. Res.*, 92, 4663–4672, <https://doi.org/10.1029/JA092iA05p04663>, 1987.
- Sivjee, G. G., Romick, G. J., and Rees, M. H.: Intensity ratio and center wavelengths of [O II] (7320–7330 Å) line emissions, *Astrophys. J.*, 229, 432–438, <https://doi.org/10.1086/156971>, 1979.
- Suzuki, H., Shiokawa, K., Tsutsumi, M., Nakamura, T., and Taguchi, M.: Atmospheric gravity waves identified by ground-based observations of the intensity and rotational temperature of OH airglow, *Polar Sci.*, 2, 1–8, <https://doi.org/10.1016/j.polar.2007.12.002>, 2008.
- Taylor, J. R.: An introduction to error analysis: the study of uncertainties in physical measurements, Second Edition, University Science Books, California, 327 pp., ISBN 9780935702422, 1997.
- Taylor, M. J., Pendleton Jr., W. R., Clark, S., Takahashi, H., Gobbi, D., and Goldberg, R. A.: Image measurements of short-period gravity waves at equatorial latitudes, *J. Geophys. Res.*, 102, 26283–26299, <https://doi.org/10.1029/96JD03515>, 1997.
- Thomas, G. E. and Olivero, J.: Noctilucent clouds as possible indicators of global changes in the mesosphere, *Adv. Space Res.*, 28, 937–946, [https://doi.org/10.1016/S0273-1177\(01\)80021-1](https://doi.org/10.1016/S0273-1177(01)80021-1), 2001.
- Wiens, R. H., Moise, A., Brown, S., Sargoytchev, S., Peterson, R. N., Shepherd, G. G., Lopez-Gonzalez, M. J., Lopez-Moreno, J. J., and Rodrigo, R.: SATI: a spectral airglow temperature imager, *Adv. Space Res.*, 19, 677–680, [https://doi.org/10.1016/S0273-1177\(97\)00162-2](https://doi.org/10.1016/S0273-1177(97)00162-2), 1997.
- Wüst, S., Bittner, M., Espy, P. J., French, W. J. R., and Mulligan, F. J.: Hydroxyl airglow observations for investigating atmospheric dynamics: results and challenges, *Atmos. Chem. Phys.*, 23, 1599–1618, <https://doi.org/10.5194/acp-23-1599-2023>, 2023.